Multidimensional NQR: Imaging and Exchange Spectroscopy*

Rainer Kimmich
Universität Ulm, Sektion Kernresonanzspektroskopie, 89069 Ulm, Germany

Z. Naturforsch. **51 a,** 330–336 (1996); received January 22, 1996

In this context a "dimension" can be of a spatial or of a spectroscopic nature. In the last two decades, multidimensional nuclear magnetic resonance and imaging have proven to be most useful tools for the investigation of materials. It turned out that some of these measuring principles can be applied to zero-field NQR as well. The purpose of this presentation is to elucidate two-dimensional exchange spectroscopy and imaging procedures suitable for NQR and to outline potential applications.

Key words: NQR, imaging, 2D exchange spectroscopy, pressure, temperature.

1. Introduction

The purpose of two- (or multi-)dimensional nuclear quadrupole resonance (NQR) experiments is to correlate information from different dimensions. A dimension can be of a spectral nature, that is, refer to a time or frequency domain, or can plainly be a spatial dimension.

In recent years diverse multidimensional NQR experiments have been suggested. This implies *2D nutation NQR spectroscopy* [1 - 3], *2D exchange NQR spectroscopy* [4, 5], and *NQR imaging* [6 - 12]. In this paper we will concentrate on the latter two schemes.

The rotating-frame NQR imaging (ρNQRI) method to be described in the following is based on nutation frequency encoding of the spatial information with the aid of gradients of the radio frequency (RF) amplitude [13]. In a sense, the evaluation formalism is closely related to that of 2D nutation NQR spectroscopy. That is, the procedures which are employed for decoding the spatial information from the acquired NQR data have a root common to both experimental schemes [2, 14].

An attractive feature of ρNQRI is that there is neither a need of a magnetic field nor of magnetic-field gradients. The applicability is restricted to solid materials permitting the record of NQR signals, of course. There is, however, no restriction with respect to the crystallinity. The evaluation formalism to be discussed in the following rather refers to materials with powder geometry.

Exchange between positions or molecular orientations with different resonance frequencies can be studied by two-dimensional exchange spectroscopy originally developed for NMR applications [15, 16]. Cross intensity reflects changes of the resonance frequency due to different line shifts or anisotropic interactions. The technique is of particular interest because information on exchange "pathways" is provided.

Analogous experiments are possible with pure NQR of polycrystalline samples [4, 5]. In comparison to 2D exchange NMR spectroscopy, there is, however, a number of additional experimental conditions and measures to be met for successful NQR experiments: NQR spectra tend to be spread over a wide frequency range. "Exchange" in the NQR case can also mean a change of the direction of quantization.

2. Rotating-frame NQR imaging (ρNQRI)

The principle of this method is to record projections of the object to be imaged. The projections refer to the direction of a gradient of the position dependent RF amplitude, that is

$$B_1 = B_1(z), \tag{1}$$

$$G_1 = \frac{\partial B_1}{\partial z}, \tag{2}$$

---

* Presented at the XIIIth International Symposium on Nuclear Quadrupole Interactions, Providence, Rhode Island, USA, July 23-28, 1995.

Reprint requests to Prof. R. Kimmich.

0932-0784 / 96 / 0500-0330 $ 06.00 © – Verlag der Zeitschrift für Naturforschung, D-72072 Tübingen

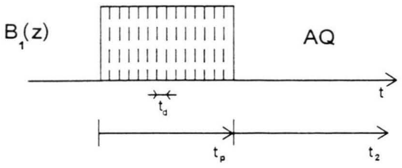

Fig. 1. ρNQRI RF pulse scheme. The pulse implies a gradient of the RF amplitude. The two time domains are the pulse width t_p and the acquisition time t_2. The pulse width is incremented in subsequent transients for nutation frequency encoding of the spatial information. The acquisition time domain probes the spectral information.

where we have assumed gradients along the z direction of the laboratory frame. We are dealing with "nutation frequency encoding" of the spatial information in contrast to "(Larmor) frequency encoding" usual in NMR imaging schemes [17].

Figure 1 shows the RF (amplitude gradient) pulse scheme for ρNQRI. The pulse is incremented either in width by t_d, the pseudo-dwell time, or equivalently in amplitude by α_d, the pseudo-dwell amplitude. Assuming resonant irradiation, the NQR signal for spins $I = 3/2$ in the presence of a B_1 gradient along the z axis is given by [18]

$$S(t_p, t_2) = \int_0^\infty \mathrm{d}z\, \rho(z)\, 2 \int_0^\pi \mathrm{d}\theta\, \sin\theta\, \frac{1}{2\pi} \int_0^{2\pi} \mathrm{d}\phi \tag{3}$$

$$\cdot \left\{ -\frac{1}{2\sqrt{3+\eta^2}}\, r(\theta,\phi) \cdot \sin[\omega_N(z) t_p]\, \sin(\omega_Q t_2) \right\}. \tag{4}$$

The polar and azimuthal angles, θ and ϕ, characterize the orientation of the RF coil axis in the field gradient tensor (FGT) eigenframe. $\rho(z)$ is the projected effective spin density as a function of the position z. The NQR line parameters are the resonance frequency ω_Q and the asymmetry parameter η. The position dependent nutation frequency $\omega_N = \omega_N(z)$ is given by

$$\omega_N(z) = \frac{\gamma B_1(z)}{2\sqrt{3+\eta^2}}\, r(\theta,\phi), \tag{5}$$

$$r(\theta,\phi) = \left\{ 4\eta^2 \cos^2\theta + [9 + \eta^2 + 6\eta\cos(2\phi)]\sin^2\theta \right\}^{1/2}. \tag{6}$$

Variation of the pulse width leads to the pseudo free-induction decay (FID)

$$\tilde{S}(t_p) = \int_0^\infty \mathrm{d}z\, \rho(z) f(z\, t_p), \tag{7}$$

where

$$f(z\, t_p) = 2 \int_0^\pi \mathrm{d}\theta\, \sin\theta\, \frac{1}{2\pi} \int_0^{2\pi} \mathrm{d}\phi \cdot \left\{ -\frac{1}{2\sqrt{3+\eta^2}}\, r(\theta,\phi) \cdot \sin[\omega_N(z) t_p]\, \sin(\omega_Q t_2) \right\}. \tag{8}$$

The substitution

$$t_p = t_d\, e^u, \tag{9}$$

$$z = z_0\, e^{-v} \tag{10}$$

leads to a convolution integral of the form

$$\tilde{S}(t_d\, e^u) = \int_{-\infty}^{\infty} \mathrm{d}v\, f_a(v) f_b(u - v), \tag{11}$$

$$f_a(v) = z_0\, e^{-v}\, \rho(z_0\, e^{-v}), \tag{12}$$

$$f_b(\zeta) = f(z_0\, t_d\, e^{\zeta}), \tag{13}$$

$$\zeta = u - v. \tag{14}$$

The experimental pseudo FID can be deconvoluted by suitable procedures such as the inverse Fourier transformation method [14] or the maximum-entropy method [2]. The result is the projection of the effective spin density of the object on the gradient direction, that is

$$\rho(z) = \frac{f_a(v)}{z}, \tag{15}$$

where $v = \ln(z_0/z)$.

B_1 gradients either can suitably be produced by surface coils, or exist in the fringe field of solenoid probes. Figure 2a shows a set-up for surface coil experiments. The resulting profile of the test object is shown in Figure 2b. This profile was corrected for the position (i. e., coil distance) dependences of the excitation and the detection sensitivity, and for the nonlinear variation of the RF amplitude intrinsic to surface

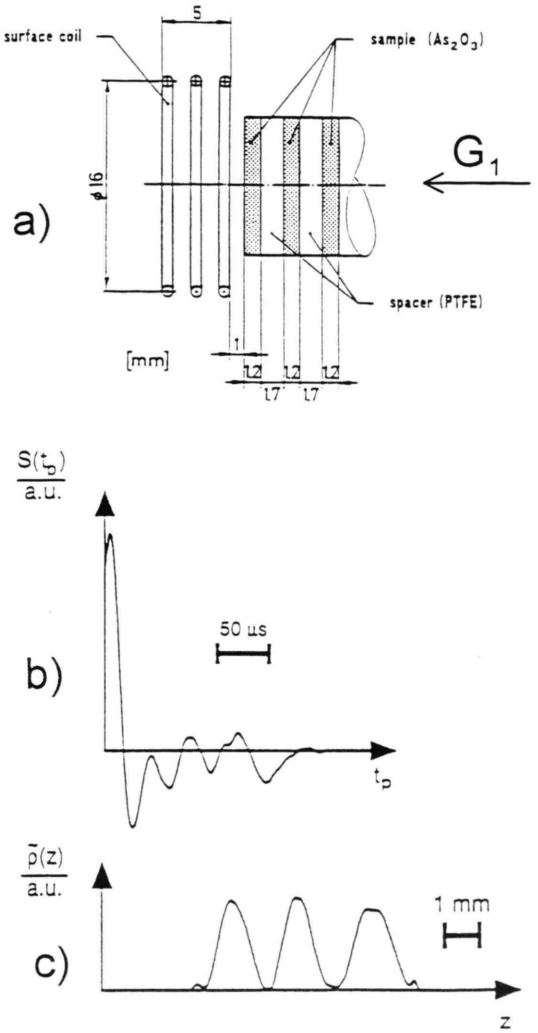

Fig. 2. ρNQRI test experiment with a $^{75}As_2O_3$ object [20]: (a) Surface coil set-up. (b) Pseudo FID recorded at 116.22 MHz using 64 pulse width increments of 3 µs each. The ordinate represents the integrated NQR line intensity. Each FID recorded in the acquisition interval consisted of 256 data points. (c) Projection (deconvoluted pseudo FID) of the spin density in the object after correction according to (16).

coils. The corrected spin density, $\tilde{\rho}$ is obtained from the evaluated spin density (15) with the aid of

$$\tilde{\rho}(z) = \rho(z)\,\frac{G_1(z)}{B_1(z)}. \qquad (16)$$

A prominent advantage of surface-coil NQR is that objects larger than the coil diameter can be investigated. Objects can thus be scanned along the surface with depth resolution in a range of the order of the coil radius.

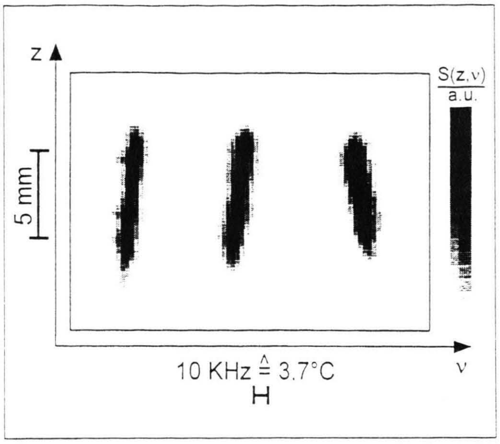

Fig. 3. Temperature gradient ρNQRI [20]. The spatial dimension, z, along the B_1 gradient is correlated with the spectral dimension, ν. The data refer to a cylindric $^{75}As_2O_3$ sample (temperature coefficient of the NQR line: –2.7 kHz/°C; room temperature resonance frequency: 116.22 MHz; asymmetry parameter: $\eta \approx 0$ [22]). The FID-s were recorded in the form of 256 data points. The RF pulse width was incremented in steps of 3 µs. The experiment was repeated several times with total temperature variations along the sample of 3 °C, 4.5 °C, and –4.5 °C (from left to right). The temperature resolution was better than 1.5 °C, the spatial resolution was better than 1 mm. The gray shades represent the signal intensity.

Two- (or three-)dimensional image data sets can be produced with the aid of a system of radio-frequency gradient coils or, preferably, by step-by-step rotation of the object relative to the B_1 gradient. For each orientation a profile across the sample is evaluated as the projection on the direction of the gradient. A projection-reconstruction formalism then permits rendering of two-dimensional NQR images of the sample [9, 19].

The ρNQRI technique is particularly suitable for the detection of gradients of physical parameters influencing the NQR line shift and of spatial distributions of the chemical composition. Examples are stress or pressure [12] and temperature gradients [21]. That is, a further dimension of a spectroscopic nature is added to the dimensions spatially resolved. Typical applications are demonstrated in Figures 3 (temperature) and 4 (pressure).

The visualization of pressure or stress distributions in objects can be based on line broadening or line shift

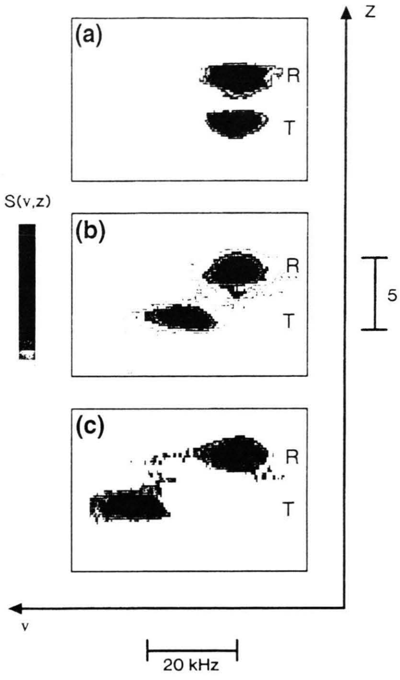

Fig. 4. Pressure ρNQRI [12]. The spatial dimension, z, along the B_1 gradient is correlated with the spectral dimension, ν. The data refer to a two-compartment object filled with lithium iodate (Li^{127}IO$_3$) which was embedded in rubber in order to avoid line broadening upon pressure exertion. The ^{127}I NQR spectra where recorded at 151.3 MHz. The images of the two-compartment arrangement (T, test compartment; R, reference compartment) shows the line shift of the test compartment depending on the pressure exerted. The pressure coefficient is 1.575 kHz/MPa [23, 24]. The gray shades correspond to the signal intensity. Without applied pressure, the frequency distribution of the spectra in the two compartments is the same (image a), whereas an external pressure selectively exerted on the test compartment causes a strong line shift toward higher frequencies (images b and c). In the latter two cases the pressure was 7 and 14 MPa, respectively, as evaluated from the line shift. Note that the linewidth essentially remains the same, independent of the exerted pressure.

effects [12]. Both phenomena can be calibrated to the experimental parameter of interest. Note however, that line shift detection of pressure requires a reasonable spectral resolution which can only be maintained if the microcrystallites are isotropically compressed. Otherwise line broadening will spoil the spectral resolution. Good results were obtained by embedding the microcrystallites in rubber before exerting the external forces.

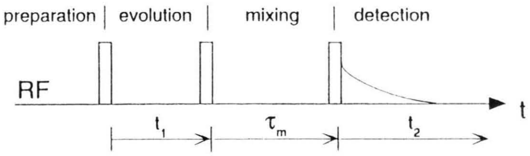

Fig. 5. RF pulse scheme for 2D exchange NQR spectroscopy. The two dimensions are represented by the time domains t_1 (to be incremented in subsequent transients) and t_2. The mixing interval τ_m is adjusted according to the exchange kinetics.

3. Two-dimensional exchange NQR spectroscopy

The technique permits the observation of exchange processes between positions with different NQR frequencies. The term "exchange" must be read in a more general sense because it does not only imply "chemical exchange" of atoms or groups but molecular rearrangements such as rotational jumps as well, provided that these motions are accompanied by NQR frequency shifts, i. e. by different electric field gradients, whatever the physical reason is.

The corresponding RF pulse sequence consists of three pulses optimized for maximal signal (Figure 5). The first pulse excites the sample assumed to be in equilibrium. The coherences produced in this way evolve in the τ_1 interval prior to the second RF pulse transferring the transverse magnetization isochromats to the longitudinal direction in part. The magnitude of these z components depends on the phase distribution achieved at the end of the evolution interval τ_1. It also depends on the component of the RF field perpendicular to the direction of the local electric field gradient. On the other hand, only the magnetization components aligned along the local electric field gradient will be "stored" and will be the potential subject of modification by exchange.

The subsequent "mixing period" τ_m is the interval in which potential exchange processes are to be investigated. The ideal condition therefore is $T_1 \gg \tau_m \gg \tau_1$, where T_1 is the spin-lattice relaxation time. After the mixing interval the longitudinal components are detected with the aid of a reading RF pulse producing a FID signal in the detection period τ_2.

τ_1 and τ_2 represent the two dimensions of the time domain from which the final 2D spectrum is derived. The length of the evolution interval τ_1 must therefore be incremented in a series of repetitions of the experiment. The increment corresponds to the dwell

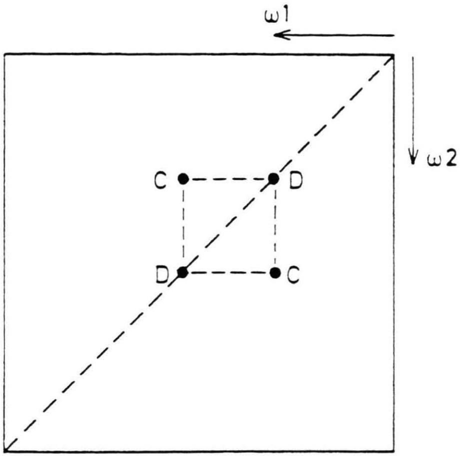

Fig. 6. Schematic 2D exchange spectrum. "Exchange" is indicated by transfer of diagonal intensity (D) to cross intensity (C).

time of the signal acquisition in the τ_2 interval. The desired two-dimensional spectrum is obtained as the two-dimensional Fourier transform, $\tilde{S}(\nu_1, \nu_2)$, of the recorded signal data set, $S(\tau_1, \tau_2)$.

Without exchange, the 2D spectrum consists solely of diagonal peaks (apart from axial peaks not of interest here). If exchange takes place in the time scale of the mixing period, additional cross-peaks arise at frequency coordinates corresponding to the sites between which the exchange occurs. Figure 6 shows a schematic representation of a 2D exchange spectrum.

The intensities of the NQR cross peaks are intrinsically weak. This is due to the powder geometry of the samples. Nevertheless, the exchange pathways are detectable and the intensities follow the theoretical expectation. Thus an exchange scheme proposed for a certain compound can be tested in an unambiguous way.

The theoretical treatment of the evolution of coherences in the course of a pulse sequence Fig. 5 can be performed on the basis of the fictitious spin-1/2 formalism [5, 25]. In the following we will give a brief outline while the complete treatment can be found in [5].

Fictitious spins-1/2, $\vec{S}'$ and $\vec{S}''$, are attributed to the spin transitions $|m\rangle \leftrightarrow |m-1\rangle$ and $|-m\rangle \leftrightarrow |-(m-1)\rangle$, respectively, where m is the magnetic quantum number. The magnetization is considered in a frame with axes ξ, η, ζ. The transverse magnetizations of the two fictitious spins-1/2 at the j^{th} site are then defined by

$$
\begin{aligned}
m'_j &= M'_{j,\xi} + iM'_{j,\eta}, && (17)\\
m''_j &= M''_{j,\xi} + iM''_{j,\eta}. && (18)
\end{aligned}
$$

The longitudinal magnetizations at the j^{th} site are designated by $M'_{j,\zeta}$ and $M''_{j,\zeta}$. The equilibrium values at the j^{th} site are $M_j^{(0)'}$ and $M_j^{(0)''}$.

Assume now that there are N sites to be distinguished in the exchange scheme with partial magnetizations as defined above. The total magnetizations may then be represented as vectors of the form

$$
\vec{m}' = \begin{pmatrix} m'_1 \\ \cdot \\ m'_j \\ \cdot \\ m'_N \end{pmatrix}, \quad \vec{m}'' = \begin{pmatrix} m''_1 \\ \cdot \\ m''_j \\ \cdot \\ m''_N \end{pmatrix} \qquad (19)
$$

and

$$
\vec{M}'_\zeta = \begin{pmatrix} M'_{1,\zeta} \\ \cdot \\ M'_{j,\zeta} \\ \cdot \\ M'_{N,\zeta} \end{pmatrix}, \quad \vec{M}''_\zeta = \begin{pmatrix} M''_{1,\zeta} \\ \cdot \\ M''_{j,\zeta} \\ \cdot \\ M''_{N,\zeta} \end{pmatrix}, \quad \vec{M}'_0 = \begin{pmatrix} M_1^{(0)'} \\ \cdot \\ M_j^{(0)'} \\ \cdot \\ M_N^{(0)'} \end{pmatrix}. \qquad (20)
$$

The effect of RF pulses can be deduced in the usual way by employing unitary transformations for rotations about the rotating-frame axis along which the RF field is aligned. The first pulse of sequence Fig. 5, for instance, may be assumed to be applied along the $+\xi$ axis so that the fictitious-spin operator S'_ζ (the treatment of which is representative for both fictitious spin-1/2 operators) is converted according to

$$
S'_\zeta \rightarrow e^{i\tilde{\alpha}S'_\xi}\, S'_\zeta\, e^{-i\tilde{\alpha}S'_\xi} = S'_\zeta \cos\tilde{\alpha} + S'_\eta \sin\tilde{\alpha}. \qquad (21)
$$

The magnetization vectors after the pulse consequently are

$$
\begin{aligned}
\vec{m}'(0+) &= i\vec{M}'_0 \sin\tilde{\alpha}, && (22)\\
\vec{M}'_\zeta(0+) &= \vec{M}'_0 \cos\tilde{\alpha}, && (23)
\end{aligned}
$$

where the matrix of the effective flip angles is

$$\tilde{\alpha} = \gamma B_1 t_p \begin{pmatrix} \lambda_1 & \cdots & 0 \\ \vdots & \ddots & \vdots \\ 0 & \cdots & \lambda_N \end{pmatrix} \tag{24}$$

γ is the gyromagnetic ratio and t_p is the pulse width. The diagonal element for the j^{th} site is given by

$$\lambda_j = \sqrt{\frac{4\eta_j^2 \cos^2\theta_j + \{9 + \eta_j^2 + 6\eta_j \cos(2\phi_j)\} \sin^2\theta_j}{3 + \eta_j^2}}, \tag{25}$$

where θ_j and ϕ_j are the polar and azimuthal angles of the coil axis in the FGT eigenframe at the j^{th} site. The asymmetry parameter at the j^{th} site is denoted as η_j.

The evolution of the magnetization vectors in an interval τ is governed by the following equations of motion:

$$\frac{d\vec{m}'(\tau)}{d\tau} = \tilde{\ell}',\ \vec{m}'(\tau) \tag{26}$$

$$\frac{d\vec{M}'_\zeta(\tau)}{d\tau} = \tilde{L}\,[\vec{M}'_\zeta(\tau) - \vec{M}'_0], \tag{27}$$

where

$$\tilde{\ell}' = i\tilde{\Omega}' - \tilde{R}'_2 + \tilde{K}, \tag{28}$$

$$\tilde{L} = -\tilde{R}_1 + \tilde{K}. \tag{29}$$

These matrices are composed of matrices for the local rotating-frame precession frequencies and the exchange rates

$$\tilde{\Omega}' = \begin{pmatrix} \omega'_1 & \cdots & 0 \\ \vdots & \ddots & \vdots \\ 0 & \cdots & \omega'_N \end{pmatrix},$$

$$\tilde{K} = \begin{pmatrix} -\sum_j k_{1j} & \cdots & k_{N1} \\ \vdots & \ddots & \vdots \\ k_{1N} & \cdots & -\sum_j k_{Nj} \end{pmatrix}. \tag{30}$$

and the matrices of the local longitudinal and transverse relaxation rates

$$\tilde{R}_1 = \begin{pmatrix} 1/T_1^{(1)} & \cdots & 0 \\ \vdots & \ddots & \vdots \\ 0 & \cdots & 1/T_1^{(N)} \end{pmatrix},$$

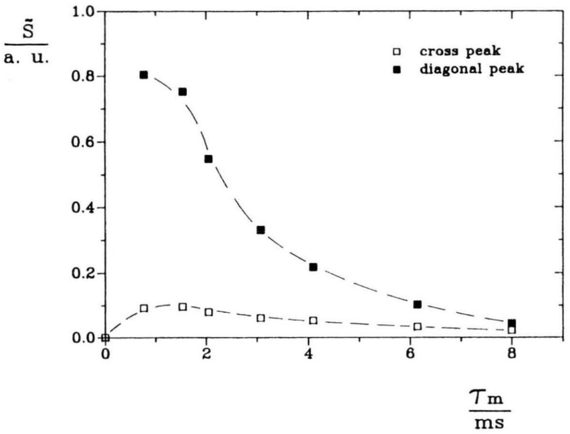

Fig. 7. Cross and diagonal intensities as a function of the mixing time τ_m. The data were evaluated from 2D exchange NQR (magnitude) ^{35}Cl spectra of the CCl$_3$ group of p-chlorobenzotrichloride at 208 K. The one-dimensional NQR spectrum consists of two lines. In order to excite both resonances at a time, the pulse sequence Fig. 5 was modified by phase alternating excitation pulses [4]. The evolution period t_1 was incremented in 128 steps of 1 µs.

$$\tilde{R}'_2 = \begin{pmatrix} 1/T_2^{(1)\prime} & \cdots & 0 \\ \vdots & \ddots & \vdots \\ 0 & \cdots & 1/T_2^{(N)\prime} \end{pmatrix}. \tag{31}$$

The solutions of the equations of motion eqns 26 and 27 are of an exponential form, i. e.,

$$\vec{m}'(\tau) = \exp\{\tilde{\ell}'\tau\}\,\vec{m}'(0), \tag{32}$$

$$\vec{M}'_\zeta(\tau) = \vec{M}'_0 - \exp\{\tilde{L}\tau\}\,[\vec{M}'_0 - \vec{M}'_\zeta(0)]. \tag{33}$$

With the above formalism, the coherence evolution in the course of the pulse sequence Fig. 5 can be deduced pulse by pulse (21) and interval by interval, (32) and (33). A suitable application example refers to the rotational isomerism of the CCl$_3$ group of p-chlorobenzotrichloride. Establishing the exchange matrix for this case and taking into account the intensity losses due to the powder geometry of the sample and due to exchange between different FGT orientations leads to a perfect description of the diagonal and cross intensity [5]. Figure 7 shows the experimental results obtained with the aid of the double side-band excitation technique, that is, the phase alternating excitation pulse (PAEP) variant of pulse sequence Figure 5 [4]. Note that not only the appearance of cross intensity is characteristic for the exchange processes, but also the strong reduction of the diagonal intensity.

4. Conclusions

The rotating-frame NQR imaging method permits one to map the local spectral properties of quadrupole nuclei. In contrast to the method proposed by Matsui et al. [6], no magnetic field gradients are used so that one is really dealing with "pure" NQR. The absence of readout gradients means in particular that the full spectroscopic information remains accessible. Applications taking advantage of this option are temperature, pressure, and stress imaging.

2D exchange NQR spectroscopy is able to reveal exchange pathways between different sites characterized by different field-gradient tensors. The cross intensity which directly reflects the exchanged population of the diverse sites generally tends to be weak relative to the NMR variant [15]. It can nevertheless be clearly detected and is thus indicative for the occurrence of exchange processes. The combined description of cross and diagonal intensity provides the full information of an exchange scheme without cut in the accuracy.

Acknowledgements

The author enjoyed a fruitful cooperation with Cecilia Gonzales, Peter Nickel, Daniel Pusiol, Hector Robert, Franz Rohmer, and Eberhard Rommel, in the course of which the work reviewed in this paper arose. Financial support of this research by the Deutsche Forschungsgemeinschaft, the Volkswagen-Stiftung, the Deutscher Akademischer Austauschdienst, and the Studienstiftung des Deutschen Volkes is gratefully acknowledged.

[1] G. S. Harbison, A. Slokenbergs, and T. M. Barbara, J. Chem. Phys. **90,** 5292 (1989).
[2] H. Robert, D. Pusiol, E. Rommel, and R. Kimmich, Z. Naturforsch. **49a,** 35 (1994).
[3] J. Dolinšek, F. Milia, G. Papavassiliou, G. Papantopoulos, and R. Rumm, J. Magn. Reson. A **114,** 147 (1995).
[4] E. Rommel, P. Nickel, F. Rohmer, R. Kimmich, C. Gonzales, and D. Pusiol, Z. Naturforsch. **47a,** 382 (1992).
[5] P. Nickel and R. Kimmich, J. Mol. Structure **345,** 253 (1995).
[6] S. Matsui, K. Kose, and T. Inouye, J. Magn. Reson. **88,** 186 (1990).
[7] E. Rommel, P. Nickel, R. Kimmich, and D. Pusiol, J. Magn. Reson. **91,** 630 (1991).
[8] K. V. Ermolaev, V. P. Tarasov, G. B. Manelis, and L. N. Erofeev, Appl. Magn. Reson. **2,** 683 (1991).
[9] R. Kimmich, E. Rommel, P. Nickel, and D. Pusiol, Z. Naturforsch. **47a,** 361 (1992).
[10] P. Nickel, E. Rommel, R. Kimmich, and D. Pusiol, Chem. Phys. Lett. **183,** 183 (1991).
[11] R. Kimmich, E. Rommel, and P. Nickel, Magn. Reson. Imaging **10,** 733 (1992).
[12] P. Nickel, H. Robert, R. Kimmich, and D. Pusiol, J. Magn. Reson. A **111,** 191 (1994).
[13] D. I. Hoult, J. Magn. Reson. **33,** 183 (1979).
[14] E. Rommel, R. Kimmich, H. Robert, and D. Pusiol, Meas. Sci. Technol. **3,** 446 (1992).
[15] J. Jeener, B. H. Meier, P. Bachmann, and R. R. Ernst, J. Chem. Phys. **71,** 4546 (1979).
[16] R. R. Ernst, G. Bodenhausen, and A. Wokaun, Principles of Nuclear Magnetic Resonance in One and Two Dimensions, Clarendon Press, Oxford 1987.
[17] P. T. Callaghan, Principles of Nuclear Magnetic Resonance Microscopy, Clarendon Press, Oxford 1991.
[18] J. C. Pratt, P. Raghunathan, and C. A. McDowell, J. Magn. Reson. **20,** 313 (1975).
[19] P. C. Lauterbur, Nature London **242,** 190 (1973).
[20] P. Nickel, Thesis, Universität Ulm, 1993.
[21] E. Rommel, D. Pusiol, P. Nickel, and R. Kimmich, Meas. Sci. Technol. **2,** 866 (1991).
[22] D. J. Treacy and P. C. Taylor, Solid State Comm. **40,** 135 (1981).
[23] D. F. Baisa and S. V. Mal'tsev, Sov. Phys. Solid State **29,** 516 (1987).
[24] F. Herlach, Helv. Phys. Acta **34,** 305 (1960).
[25] A. Abragam, The Principles of Nuclear Magnetism, Clarendon Press, Oxford 1961.